processes

MDPI

Article

An Investigation of MnO_x and K/MnO_x-Based Catalysts on MnO_2 and Fe_3O_4 Supports for the Deep Oxidation of Cyclohexane

Md Sarwar Kamal [1], Catherine B. Almquist [2,*] and David L. Tierney [3]

[1] Department of Chemical and Biomolecular Engineering, Case Western Reserve University, Cleveland, OH 44106, USA; mxk1569@case.edu
[2] Department of Chemical and Biomedical Engineering, Miami University, Oxford, OH 45056, USA
[3] Department of Chemistry and Biochemistry, Miami University, Oxford, OH 45056, USA; dtierney@miamioh.edu
* Correspondence: almquic@miamioh.edu; Tel.: +1-513-529-0767

Abstract: K/MnO_x catalysts on MnO_2 and Fe_3O_4 supports were synthesized and compared for the deep oxidation of cyclohexane. The presence of potassium (K) on the catalysts enhanced the catalytic activity compared to catalysts with similar composition but without K. Interestingly, the lowest loading of K/MnO_x used in this study (0.63 mmoles/g support) performed better than those with higher loadings. The presence of K on the catalysts increased water adsorption, decreased the extent of sintering, and inhibited changes in crystal phase of the catalyst support, as evidenced by TGA, XRD, and BET surface area analyses. The XRD profiles of the catalysts showed mixed crystal phases of MnO_x and FeO_x species, and EPR results support the presence of mixed valence states of Fe and Mn. The activation energies for MnO_x-supported catalysts and FeO_x-supported catalysts were approximately 50 kJ/mole and 53 kJ/mole, respectively.

Keywords: K/MnO_x; MnO_x; FeO_x; cyclohexane; catalytic oxidation

check for updates

Academic Editor: Christos Argirusis

Received: 7 January 2025
Revised: 11 February 2025
Accepted: 21 February 2025
Published: 24 February 2025

Citation: Kamal, M.S.; Almquist, C.B.; Tierney, D.L. An Investigation of MnO_x and K/MnO_x-Based Catalysts on MnO_2 and Fe_3O_4 Supports for the Deep Oxidation of Cyclohexane. *Processes* **2025**, *13*, 634. https://doi.org/10.3390/pr13030634

Copyright: © 2025 by the authors. Licensee MDPI, Basel, Switzerland. This article is an open access article distributed under the terms and conditions of the Creative Commons Attribution (CC BY) license (https://creativecommons.org/licenses/by/4.0/).

1. Introduction

Volatile organic compounds (VOCs) have detrimental impacts on both human health and the environment [1–3]. According to Ian Tiseo (2024), the United States emitted approximately 12.5 million tons of volatile organic compounds (VOC) in 2023 [4]. Not only do VOCs directly contribute to high healthcare costs [5], but VOCs actively participate in atmospheric photochemical reactions that result in secondary pollutants, such as ozone and peroxyacetyl nitrates (PANs) [6,7]. These compounds can be more harmful to human health than VOCs, and the resulting urban haze that they create can be damaging to the environment.

There are several methods used to remove VOC emissions from industrial sources, including those that recover the VOCs, those that destroy the VOCs, and combinations of both [8]. The selection of emissions control for VOCs often depends upon the volumetric flow rate of the gas stream, the concentration of the VOCs, safety, and ultimately, the relative cost effectiveness of the VOC control strategies. VOCs can be recovered using adsorption, absorption, condensation, and membrane separation processes. VOC destruction methods are often used for high-volume low-concentration streams, and they include thermal and regenerative thermal oxidation, catalytic oxidation, and biological treatment [8]. The most typical method used for VOC destruction in air is regenerative thermal oxidation [9]. In

regenerative thermal oxidation, heat energy is recovered by cycling the inlet gases and combustion effluent gases through packed beds of ceramic materials. However, thermal oxidation requires very high temperatures, up to 1200 °C for some hazardous waste incinerators [10], and the combustion of fossil fuels is required to achieve such high temperatures. Additionally, thermally formed nitrogen oxides (NO_x) can be formed in high-temperature combustion processes.

Catalytic oxidation of VOCs is attractive as a method to destroy VOCs because it reduces the amount of energy required compared to thermal oxidation. A catalyst reduces the activation energy of a chemical reaction, which allows the reaction to proceed at lower temperatures. Consequently, the lower temperatures in catalytic oxidation of VOCs reduce the consumption of fossil fuels and lower the formation of thermal NO_x.

The catalytic oxidation of VOCs has been studied using a variety of catalysts, and several review articles have been published [11–18]. The catalysts investigated for the catalytic oxidation of VOCs include noble metals, non-noble metal oxides, and mixed-metal oxides. Noble metal catalysts have very high catalytic activity for VOC oxidation. However, they are expensive and can become deactivated during industrial use by sintering and poisoning. Therefore, non-noble metal catalysts are more attractive for removing VOC emissions due to their comparatively lower cost and stability.

Among various non-noble metal oxide catalysts, manganese oxide (MnO_x) catalysts demonstrate significant activity for VOC oxidation [14–16,18–26]. The high activity can be associated with multiple valence states of Mn, mobile surface oxygen species, and lattice oxygen participation in the reaction [16,18–26]. The Mars-van Krevelen (MVK) catalytic mechanism for VOC oxidation is often used to describe MnO_x catalysts because of the mobility of the lattice oxygen atoms in their structure [26]. In this mechanism, the VOC interacts with a lattice oxygen atom and removes it from the catalyst surface [19,25,26]. This creates oxygen vacancies on the catalyst surface, which are subsequently filled by gaseous oxygen molecules.

Potassium (K) doping of catalysts has been shown to enhance the stability and improve the catalytic activity of catalysts for VOC oxidation [27–32]. Promotion effects include increasing surface-active species, improving the dispersion of the active metal catalyst, improving redox properties, modifying the crystal structure of the catalyst, and improving the thermal stability of the catalyst. However, the promotional effects of K on MnO_x catalysts are dependent upon the extent of K loading and their intended application. For example, in 2020 Lai et al. [31] found that the catalytic activity for the catalytic oxidation of toluene on $Mn/Ce_{0.65}Zr_{0.35}O_2$ increased with increasing loadings of K up to 0.2 K/Mn molar ratio but decreased at higher K loadings [31]. They concluded that the addition of K promoted the reducibility of the catalysts, facilitated the formation of more surface adsorbed oxygen on the catalyst surface, generated more oxygen vacancies, and enhanced the oxygen mobility. At K/Mn molar ratios higher than 0.2, the catalytic activity likely decreased due to blocking of the active sites on the catalyst [31]. In 2023 Greluk et al. [32] found that K-doping enhanced the stability of the Co/MnO_x catalysts for steam reforming of ethanol by lowering the carbon build-up on the catalyst surface [32]. They concluded that a role of K-doping was to enhance the adsorption–dissociation of water molecules, and hence, the direct oxidation of carbonaceous species on the surface of the catalyst [32].

In further support of the promoter effect of K on MnO_x catalysts, it has been found that cryptomelane is an active VOC oxidation catalyst [32–44]. Cryptomelane is an octahedral molecular sieve (OMS-2) that has a 2 × 2 square tunnel structure with a pore size of about 4.6 Å, and it has a stoichiometric formula of approximately KMn_8O_{16} [45]. The activity of cryptomelane has been reported to be a result of the mixed valence state of the manganese (Mn) and the mobility of the lattice oxygen in the cryptomelane surface structure [32–44].

In a review by Suib [45], it is stated that mixed valence is important in electron transfer, energy transfer, and redox catalysis and that oxygen vacancies are related to potential catalytic activity.

Supported MnO_x catalysts have also been studied for VOC oxidation reactions [20,26,35,46–52]. Catalyst supports can have a significant impact on the activity of MnO_x catalysts for many reasons, including changes in surface area; distribution of active species; catalyst-support interactions; reducibility; adsorption–desorption properties for the VOCs, oxygen, water vapor, and CO_2; and changes in surface oxygen species and their mobilities. However, the application in which the supported MnO_x is used must be considered. For example, Liu et al. [48] compared the catalytic activity for the oxidation of chlorobenzene of supported MnO_x catalysts on TiO_2, Al_2O_3, and SiO_2 and found that MnO_x/TiO_2 had the highest activity. The dispersion of Mn and its stability in the presence of chlorinated compounds was provided as possible reasons for this observation. However, Gallardo-Amores et al. [49] found that supported MnO_x on anatase TiO_2 has less activity for the oxidation of 2-propanol than unsupported MnO_x catalysts. It was concluded that the dissolution of Mn active sites by TiO_2 was the reason for the lower activity of the supported catalysts compared to the unsupported catalysts [49]. Jung, et al. [47] investigated the role of the support (Al_2O_3, SiO_2, and TiO_2) for MnO_x catalysts for the oxidation of benzene, toluene, and xylene vapors. They found that MnO_x supported on γ-Al_2O_3 had a higher catalytic activity than MnO_x on the other supports that were investigated. They concluded that defect oxides played a predominant role in the catalytic activity compared to surface area, acidity, and lattice oxygen mobility [47].

FeO_x-supported MnO_x catalysts have been investigated for VOC oxidation [50–53]. Duplancic et al. [50] investigated the catalytic oxidation of toluene on MnO_x catalysts on FeO_x, NiO_x, and CuO_x. They found that Mn/FeO_x had the highest catalytic activity for toluene oxidation of those catalysts studied, and the activity was comparable to a commercial Pt/Al_2O_3 catalyst. The observed catalytic activities correlated with the predicted binding energy of toluene adsorption on the surface of the catalysts [50]. Gong et al. [53] found that the composite of FeO_x/MnO_x had higher catalytic activity for the degradation of chlorobenzene than MnO_x alone. The FeO_x altered the redox properties of the MnO_x catalyst [53]. Soltan et al. [52] found that MnO_x/FeO_x composite catalysts had higher activity for toluene oxidation than MnO_x or FeO_x alone. They concluded that the synergistic effects of dual oxygen vacancies enhanced the catalytic activity for toluene oxidation [52]. This is supported by Li et al. [54] who used XPS results to show that redox reactions between Fe and Mn may occur at the surface of MnO_x/FeO_x composite catalysts [54].

In this study, the catalytic activities of K/MnO_x catalysts and MnO_x catalysts were compared for the deep oxidation of cyclohexane vapor. While the selective oxidation of cyclohexane to cyclohexanol and cyclohexanone (KA oil) has been extensively studied in support of the production of adipic acid (an important precursor to nylon), the deep oxidation of cyclohexane vapor has been published less often in the recent literature. In this study, cyclohexane vapor was used as a representative VOC for the comparison of catalyst activities.

The specific objectives of this research were as follows: (1) compare the effects of the support (Fe_3O_4 and MnO_2) on the performance of K/MnO_x-based catalysts; (2) investigate the effect of K on catalyst characteristics and catalytic activities; and (3) investigate the effect of K/MnO_x loadings on catalytic performance for Fe_3O_4- and MnO_2-supported catalysts. Efforts to meet these objectives are described in the ensuing sections.

2. Materials and Methods

2.1. Materials

The following materials were used in this study: cyclohexane, potassium permanganate and manganese (II) acetate tetrahydrate (Alfa Aesar, now Thermo Fisher Scientific, Waltham, MA, USA); iron oxide (Fe_3O_4), nano powder (<50 nm), and activated manganese (IV) oxide (β-MnO_2) (Sigma-Aldrich, St. Louis, MO, USA).

2.2. Catalyst Synthesis Methods

The catalysts were prepared using a wet-incipient method. The process is shown in Figure 1. In brief, 2 g of metal oxide support was added to 50 mL of deionized (DI) water, and the slurry was stirred with a magnetic stirrer for five minutes. Fe_3O_4 and activated MnO_2 were used as the metal oxide supports. Then, a measured amount of $KMnO_4$ was added to the slurry. The slurry was heated to about 80 °C and stirred continuously until the slurry became a thick paste. This paste was then dried overnight at 125 °C. Using a mortar and pestle, the dried sample was crushed to a fine powder, and the resulting powder was calcined for two hours at 700 °C in a furnace. Following calcination, the powders were again crushed with a mortar and pestle to form a fine powder. The support materials and two additional catalysts prepared using manganese acetate (MAc) as the precursor on the Fe_3O_4 support were also processed in a similar manner. A summary of catalysts that were prepared for this study is provided in Table 1.

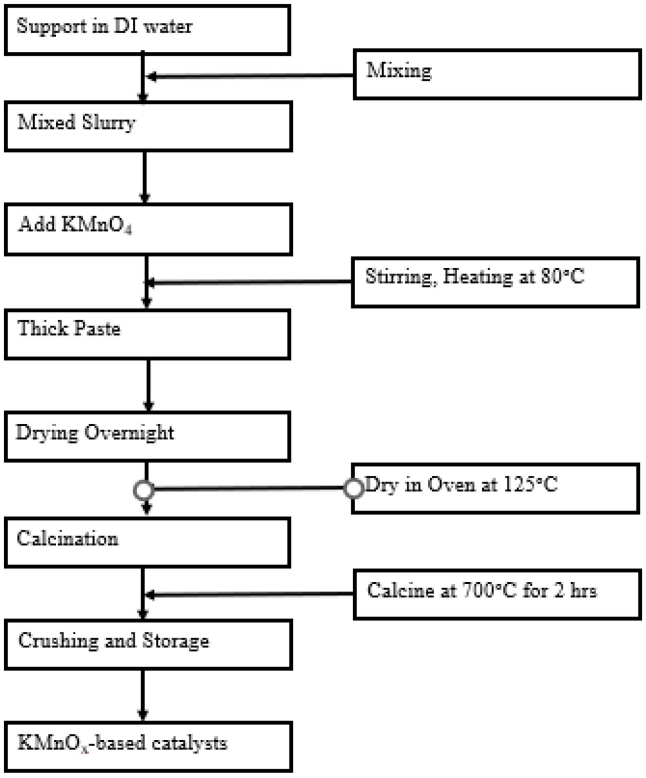


Figure 1. Overview of catalyst synthesis process.

$KMnO_4$ is an oxidizing agent, and so its addition to Fe_3O_4 and β-MnO_2 will result in catalysts with Mn and Fe in mixed oxidation states. In the synthesis method, the potassium is retained and would be distributed onto the surface of the catalysts. The support structures change crystallinity and crystal phase following calcination. Therefore, the supports will be referred to as FeO_x and MnO_x, since the crystal phases of the supports following calcination are mixed oxides.

Table 1. Inventory of catalyst samples synthesized for this study.

Identification	Support (as Purchased)	K/MnO_x Loading (mmole/g Support)	Nominal Composition [1] (Molar Ratios)		
			K/Fe	Mn/Fe	K/Mn
FeO_x supported catalysts					
FO-C	Fe_3O_4	0	0	0	N/A
KM-FO-1	Fe_3O_4	0.63	0.049	0.049	1
KM-FO-2	Fe_3O_4	1.58	0.122	0.122	1
KM-FO-3	Fe_3O_4	2.53	0.195	0.195	1
MAc-FO-1	Fe_3O_4	0.63 (Mn only)	0	0.049	0
MAc-FO-2	Fe_3O_4	1.58 (Mn only)	0	0.122	0
MnO_x-supported catalysts					
MO-C	Activated MnO_2	0	N/A	N/A	0
KM-MO-1	Activated MnO_2	0.63	N/A	N/A	0.052
KM-MO-2	Activated MnO_2	1.58	N/A	N/A	0.121
KM-MO-3	Activated MnO_2	2.53	N/A	N/A	0.182

[1] Nominal composition is based upon measured amounts of $KMnO_4$ added to the catalyst support. EDS analyses are provided in the Supplementary Documentation to support the reported elemental molar ratios.

2.3. Catalyst Characterization

The catalysts were characterized to assess their chemical and physical properties. Each type of characterization that was conducted is described below.

2.3.1. Brunauer–Emmett–Teller (BET) Surface Area

A Micromeritics TriStar II surface area analyzer (Norcross, GA, USA) was used to measure the surface area, pore volume, and pore size of the catalysts after calcination and of the supports both before and after calcination. The BET surface area was determined using nitrogen adsorption at 77 K. Pore size and pore volume were determined by the Barrett–Joyner–Halenda (BJH) model.

2.3.2. X-Ray Diffraction (XRD)

The crystal phases and crystallinity of the catalysts were assessed on the catalysts used in this study using a Bruker D8 Advance powder X-ray diffractometer (Billerica, MA USA). Data on the instrument was collected from $2\theta = 5^\circ$ to 80°, with a step size of 0.01° at 0.1 s per step. Bruker software, DiffracEva, and the Powder Diffraction File (PDF) database, were used for phase identification.

The crystallite sizes of the predominant Mn oxide species were calculated using the Scherrer equation (Equation (1)) and the XRD profiles at $2\theta = 12.8^\circ$, which is representative of cryptomelane-based materials [55].

$$L = \frac{K\lambda}{FWHM * cos\theta} \quad (1)$$

In Equation (1), L is the crystallite size (nm), λ is the incident wavelength of 0.154 nm, θ is the angle in radians, $FWHM$ = full width at half maximum (radians), and K is a shape factor that was taken to be 0.9 for this study. To find $FWHM$, OriginPro 2024 (Northampton, MA, USA) was used, which utilizes the Lorenz system for nonlinear curve fitting from gadgets by employing Quick Fit.

2.3.3. Scanning Electron Microscope (SEM) and Energy Dispersive Spectrometry (EDS)

A Zeiss Supra 35 variable pressure FEG SEM (Oberkochen, Germany) was used to investigate the morphologies of the catalysts. The images were taken at 75,000× magnification, 3 KeV EHT, 6 mm to 8 mm working distance (WD), and 30 µm standard aperture.

The SEM is equipped with an EDAX Genesis 2000 energy dispersive spectrometry (EDS) detector (MahWah, NJ, USA). EDS was used to provide information regarding the elemental composition of each catalyst. The spectra were taken at 15 KeV and 10 mm WD with an aperture size of 60 µm. Bruker Esprit v.2.1 software was used for elemental analysis by the quantification model of the Phi (Rho, Z) method. These data are provided in Supplemental Information.

2.3.4. Thermal Gravimetric Analyses (TGA)

Thermal gravimetric analyses (TGA) were conducted on all catalysts using a TA Instruments Q500 TGA (New Castle, DE, USA). The temperature was ramped at 10 °C/min from ambient temperature to 900 °C under a nitrogen gas atmosphere. A platinum pan was used as the sample holder.

2.3.5. Fourier Transform Infrared (FTIR) Spectrometry

FTIR experiments were conducted on a Thermo Nicolet NEXUS 670 FTIR spectrometer (Thermo Fisher Scientific, Waltham, MA, USA) to evaluate the functional organic groups on both fresh and previously used catalysts. The catalysts were scanned in the 400 to 4000 cm^{-1} range at a resolution of 4 cm^{-1} on the spectrometer. Finely powdered samples were dispersed in potassium bromide (KBr), which is optically transparent in FTIR. The FTIR spectra were analyzed by comparison with an Infrared Spectroscopy Absorbance table [56].

2.3.6. Electron Paramagnetic Resonance (EPR)

A Bruker EMX spectrometer (Billerica, MA, USA) equipped with an ER041xG microwave bridge and an ER4119-HS cavity at Miami University Ohio's Advanced EPR Laboratory was used to collect CW-EPR spectra. EPR was used to study the electronic properties of the catalyst. The samples were placed in a quartz X-Band EPR tube of 4 mm OD and 250 mm in length. The spectra were recorded at room temperature by signal-averaging 2 scans with 7600 G central field, 15,000 G sweep width, 100 s sweep time, 5 G modulation amplitude (100 kHz), and 0.02 mW microwave power (9.4 GHz) [57].

2.4. Catalyst Performance Tests

The test system used in this study, depicted in Figure 2, consists of a stainless-steel tubular reactor (ID = 0.32 cm), a diffusion cell to generate cyclohexane vapors, a mass flow controller (MKS Instruments, model no. M100B12CS1BV, Andover, MA, USA) to control the flow rate of air, and a Lindberg/Blue Mini-Mite tube furnace to control the reaction temperature.

For each experimental trial, the performance of the catalyst was investigated using 50 mg of catalyst that was secured with quartz wool in the middle of the reaction tube. Air, flowing at 50 cubic centimeters per min (ccpm), was mixed with cyclohexane vapors from the diffusion cell and was directed through the tubular reactor. The flow of air was measured before and after each experimental trial using a bubble meter. A gas-tight 100 µL Hamilton syringe was used to collect the effluent from the reactor for analysis on an Agilent 6890N gas chromatograph (GC) (Agilent Technologies, Santa Clara, CA, USA) equipped with a flame ionization detector (FID). The first readings were taken in triplicates at 100 °C and were collected at least two hours after the reaction temperature was reached. Then, subsequent reaction temperatures were investigated over the range of 150 °C to 400 °C.

The test system was allowed to equilibrate for at least 30 min at each reaction temperature before gas samples were collected. An empty reactor tube was analyzed with a similar reaction setup to evaluate cyclohexane degradation without a catalyst.

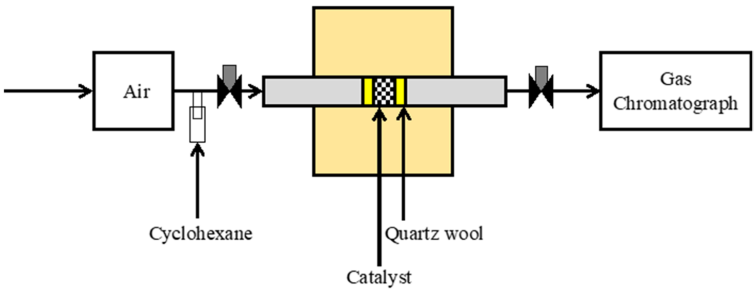


Figure 2. Schematic of the test system used for catalyst performance analysis.

Chemstation software (Agilent Technologies, Santa Clara, CA, USA) was used to obtain chromatographs and peak areas from the flame ionization detector (FID). A calibration curve was made to correlate the peak areas with cyclohexane concentration in air. An Amprobe CO_2-100 CO_2 meter (Everett, WA, USA) was used to measure the concentration of CO_2 in the reactor effluent. The CO_2 measurements were recorded to determine the carbon balance. For selected catalysts, the catalyst activity was assessed for 95 h of continuous operation at 350 °C, 375 °C, and 400 °C.

3. Results

3.1. Catalyst Characteristics

The BET surface area, micropore area, pore width, pore volume, and average crystallite size data for each catalyst are summarized in Table 2. Following calcination, the surface areas of Fe_3O_4 and β-MnO_2 decreased significantly. This result is expected since calcination at 700 °C would cause the catalyst particles to agglomerate and sinter. The addition of K/MnO_x to the FeO_x support decreased the extent of sintering, as indicated by the higher surface areas of the KM-FO-X (where X = 1, 2, or 3) catalysts compared to FO-C and MAc-FO-X catalysts. The pore widths of the catalysts with K/MnO_x on FeO_x were similar to that of the Fe_3O_4 as purchased, while the pore volumes decreased proportionally to surface area. The MnO_x crystal size was not affected significantly with increasing K/MnO_x loadings on FeO_x. The addition of manganese acetate to the FeO_x support appeared to have very little impact on catalyst sintering, since the surface areas, pore widths, and pore volumes of MAc-FO-1 and MAc-FO-2 catalysts are similar to those of FO-C.

Table 2. Summary of surface areas, pore width, pore volume, and crystallite size.

Catalyst ID	BET Surface Area (m^2/g)	Micropore Area [3] (m^2/g)	Pore Width [4] (nm)	Pore Volume [4] (cm^3/g)	Mn-Species Crystallite Size [5] (nm)
			FeO_x-supported catalysts		
FO-AP [1]	40	9.9	35.1	0.39	N/A
FO-C [2]	14.2	2.6	12.3	0.04	N/A
KM-FO-1	19.6	2.2	34.5	0.17	66
KM-FO-2	24.1	3.5	34.8	0.20	62
KM-FO-3	22.8	3.8	34.5	0.18	61
MAc-FO-1	12.4	1.1	13.7	0.04	N/A
MAc-FO-2	11.6	0.7	14.1	0.04	N/A

Table 2. *Cont.*

Catalyst ID	BET Surface Area (m^2/g)	Micropore Area [3] (m^2/g)	Pore Width [4] (nm)	Pore Volume [4] (cm^3/g)	Mn-Species Crystallite Size [5] (nm)
			MnO_x-supported catalysts		
MO-AP [1]	80.6	0	7.1	0.17	N/A
MO-C [2]	8.7	0.9	17.9	0.03	N/A
KM-MO-1	9.2	0.8	26.9	0.06	54
KM-MO-2	8.1	2.6	40	0.07	36
KM-MO-3	7.3	2.7	38.3	0.07	29

N/A = no XRD peak at 2θ = 12.8°. [1] AP: as purchased. [2] all samples except those that are as purchased were calcined at 700 °C for 2 h. [3] calculation methods provided in supporting documentation [58–63]. [4] Based on BJH model using the desorption of N_2 from the catalysts at 77 K. [5] Based on Scherrer Equation and XRD peak at 2θ = 12.8°.

The addition of $KMnO_4$ to β-MnO_2 had very little effect on the surface area following calcination, as indicated by the similar surface areas of MO-C and KM-MO-X catalysts. However, the micropore area, pore width, and pore volumes increased with the addition of K/MnO_x compared to those of MO-C, and the crystal size of the K/Mn species (based on 2θ = 12.8°) decreased from 54 nm to 29 nm with increasing K loadings from 0.63 mmoles/g support to 2.53 mmoles/g support.

Figure 3 shows the XRD profiles of FeO_x-based catalysts. The XRD profiles of Fe_3O_4 as purchased and that of the support following calcination at 700 °C for 2 h (FO-C) show that the support underwent a crystal phase transformation from Fe_3O_4 to α-Fe_2O_3. However, the XRD profiles of the KM-FO-X catalysts show peaks that are representative of both Fe_2O_3 (2θ = 24.2°, 33.2°, 41.2°, and 49.4°) and Fe_3O_4 (2θ = 30.1° and 43.2°), indicating that the Fe in the sample has mixed valence states. As K/MnO_x loading increases, XRD peaks that are representative of Fe_3O_4 increase, while those representative of Fe_2O_3 decrease. In addition, peaks associated with K/MnO_x species appear in XRD profiles of KM-FO-X catalysts at 2θ = 12.8° and 25.6°, and they increase with increasing loadings of K/MnO_x. These peaks represent the formation of birnessite (δ-MnO_2) on FeO_x, which is supported by Birkner and Navrotsky (2017) who published XRD patterns for both birnessite and cryptomelane (α-(K)MnO_2) [64]. At the highest K/MnO_x loading in this study (KM-FO-3), Fe_3O_4 appears to be the dominant crystal phase in the FeO_x support. These results indicate that the addition of K/MnO_x suppresses the extent of crystal phase change from Fe_3O_4 to Fe_2O_3. Sintering and crystal phase changes occur by mass transport processes at the grain boundaries between particles [65]. The addition of K, then, may interfere with the grain boundary diffusion, thus inhibiting sintering and crystal phase changes.

In Figure 4, the XRD profiles of the catalysts prepared with manganese acetate on FeO_x are shown. In these catalysts, the phase change from Fe_3O_4 to α-Fe_2O_3 occurs following calcination. There are no noticeable peaks associated with Fe_3O_4 in FO-C, MAc-FO-1, and MAc-FO-2 catalysts. In addition, there are no noticeable peaks that are associated with MnO_x in the XRD profiles of MAc-FO-1 and MAc-FO-2. This indicates that the MnO_x species on these catalysts are either amorphous or they are present below the detection limits of the XRD. A comparison of Figures 3 and 4 shows that the addition of K to the catalysts inhibits phase transformation of the catalyst support and promotes the crystallization of the K/MnO_x species on the surface of the catalyst.

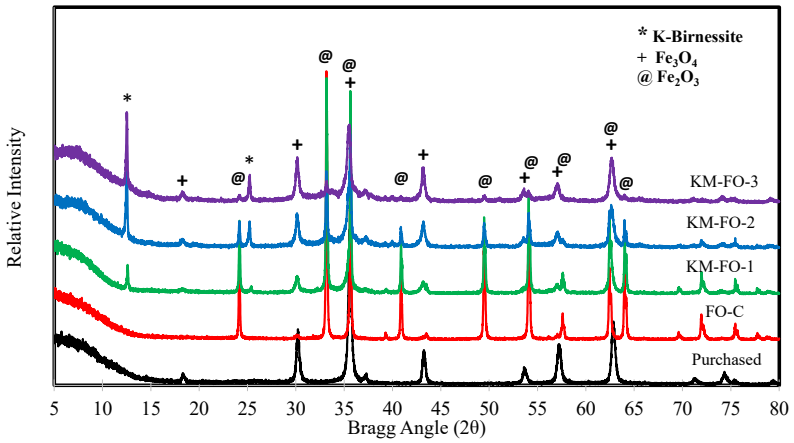


Figure 3. XRD profiles for FeO_x-supported K/MnO_x catalysts.

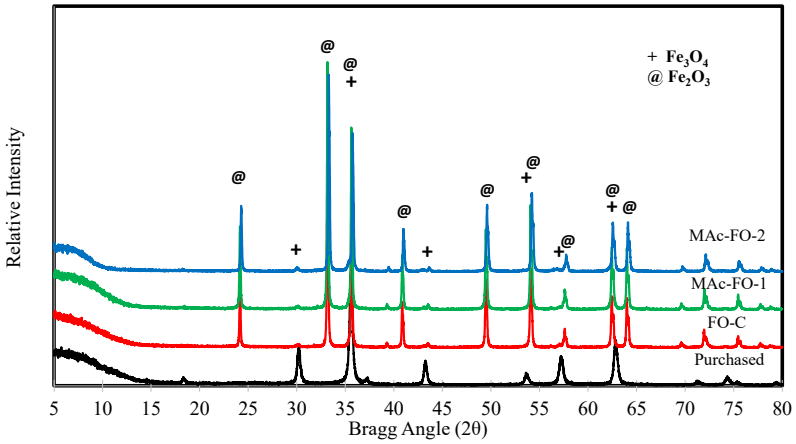


Figure 4. XRD profiles of the FeO_x-supported MnO_x catalysts.

Figure 5 shows the XRD profiles for the K/MnO_x catalysts. The activated MnO_2 (as purchased) is weakly crystalline (β—MnO_2), as indicated by the relatively broad and weak intensity peaks in the XRD profile at 2θ = 37.5°, 42.5°, and 55°. However, after calcination, a crystal phase transformation to Mn_2O_3 was apparent in sample MO-C, represented by peaks at 2θ = 23.4°, 32.9°, 38.5°, and 57°. The XRD profiles for KM-MO-X catalysts show mixed MnO_x crystalline species, with peaks representing both Mn_2O_3 and cryptomelane (2θ = 12.8°, 18.3°, 26°, 29°, 37.2°, and 42°). The cryptomelane peaks increased with increasing K/MnO_x loading.

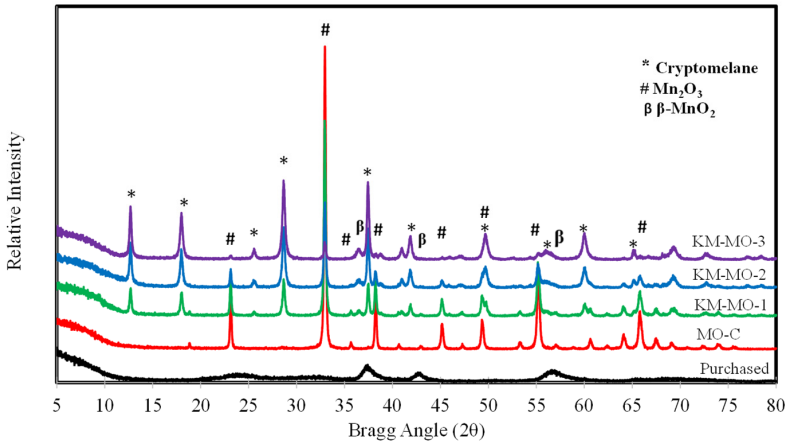


Figure 5. XRD profiles for unsupported K/MnO_x catalysts.

SEM images were acquired to investigate the morphological structures of the catalysts. Figures 6 and 7 show the SEM micrographs of the FeO_x-supported catalysts. FO-C and KM-FO-1 (Figure 6a,b) have similar surface structures resembling sintered particles in the shape of small elbows. However, the KM-FO-1 (Figure 6b) catalyst has more particle agglomeration than the FO-C catalyst, and it has some precipitate on its surface, indicated by orange-colored arrows. The KM-FO-2 (Figure 6c) catalyst also displays agglomerated particles and precipitate on the surface of the catalyst. Larger structures start to appear, as indicated by the green arrows. The KM-FO-3 (Figure 6d) catalyst has a slightly different surface than KM-FO-2. The precipitate over the surface is predominant, and the larger structures have become more apparent, again shown by the green arrows. These new plate-like structures likely indicate the presence of K-Birnessite, which is supported by the XRD profiles of KM-FO-X catalysts.

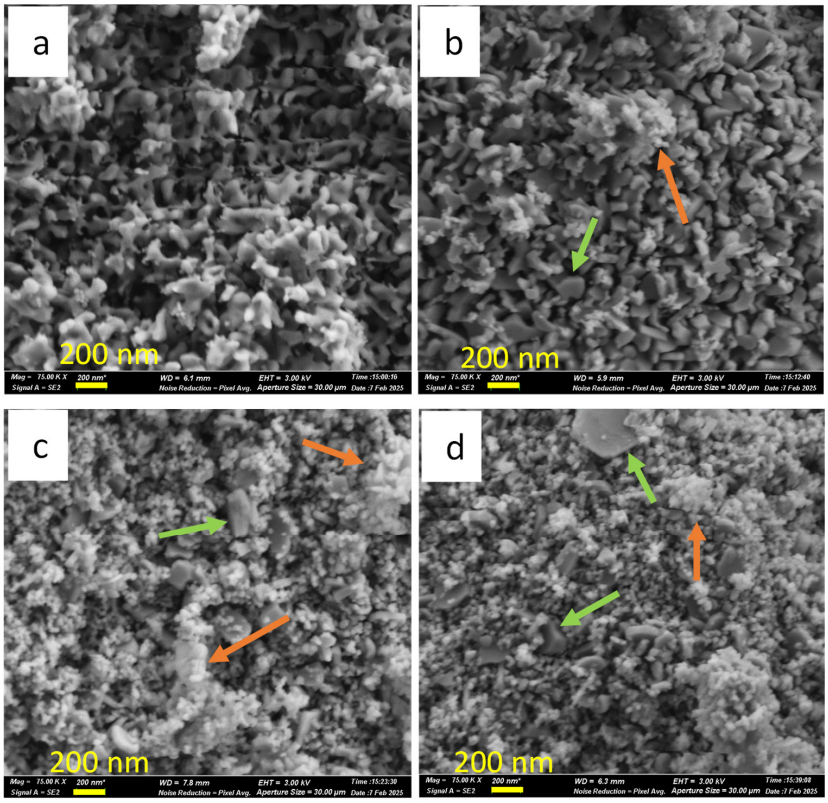


Figure 6. SEM micrographs of (**a**) FO-C, (**b**) KM-FO-1, (**c**) KM-FO-2, (**d**) KM-FO-3. 75,000X; WD between 6 mm and 8 mm; EHT = 3 kV.

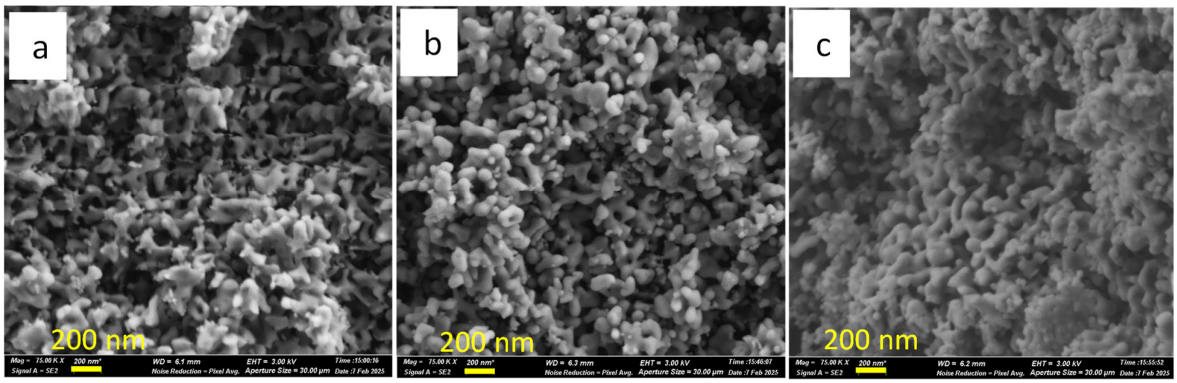


Figure 7. SEM micrographs of (**a**) FO-C, (**b**) MAc-FO-1, (**c**) MAc-FO-2. 75,000X; WD = 6 mm; EHT = 3 kV.

SEM micrographs MAc-FO-1 and MAc-FO-2 were also compared with FO-C, as displayed in Figure 7a–c. These images show the same morphology as FO-C (Figure 7a), but they appear to be more sintered than the KM-FO-X catalysts.

SEM micrographs of KM-MO-X catalysts are shown in Figure 8. MO-C (Figure 8a) has a porous structure, and it contains some rod-like crystal structures that extrude out from the porous matrix. As K/MnO_x is added to the catalysts, the formation of nanorod-like structures become more prominent. These nanorod or needle-like structures are similar to those reported for cryptomelane [19,42], which supports the XRD data regarding the formation of cryptomelane with the addition of K to MnO_x.

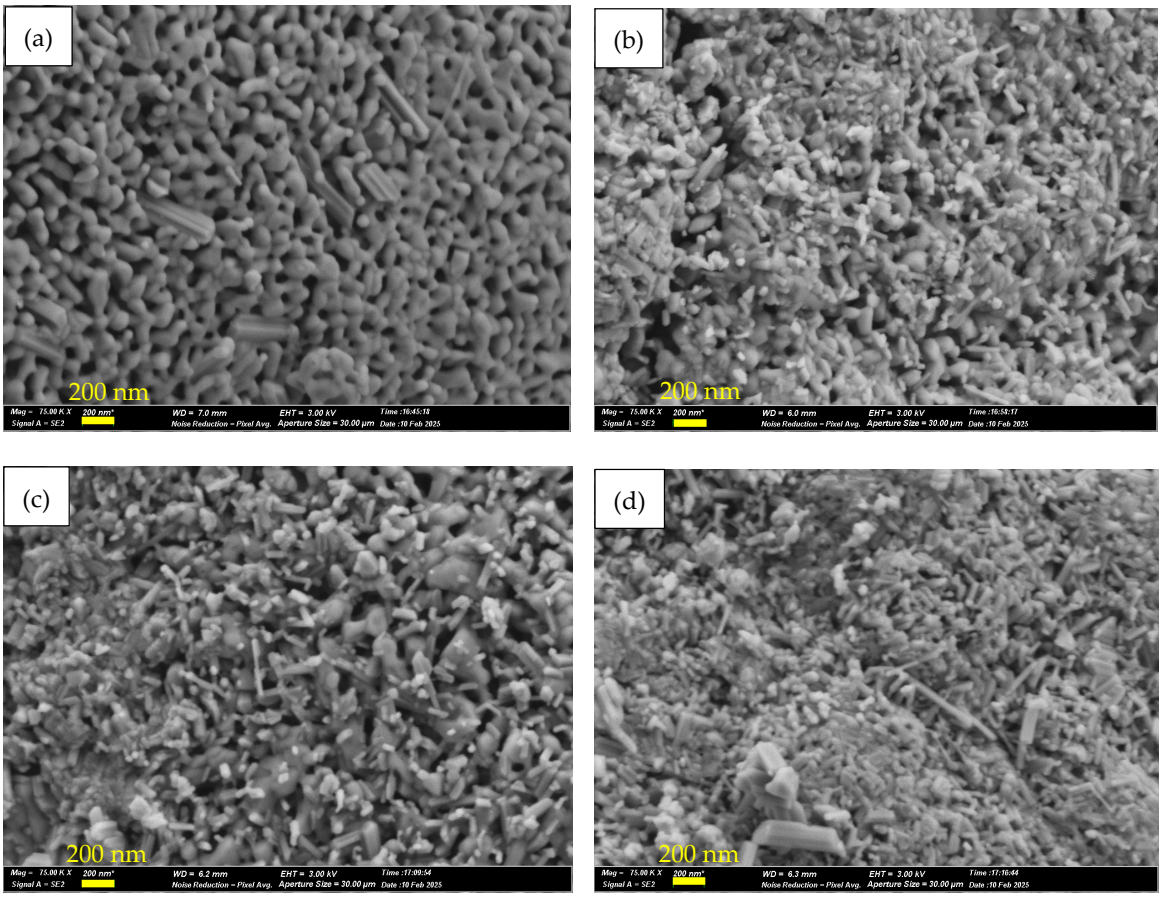
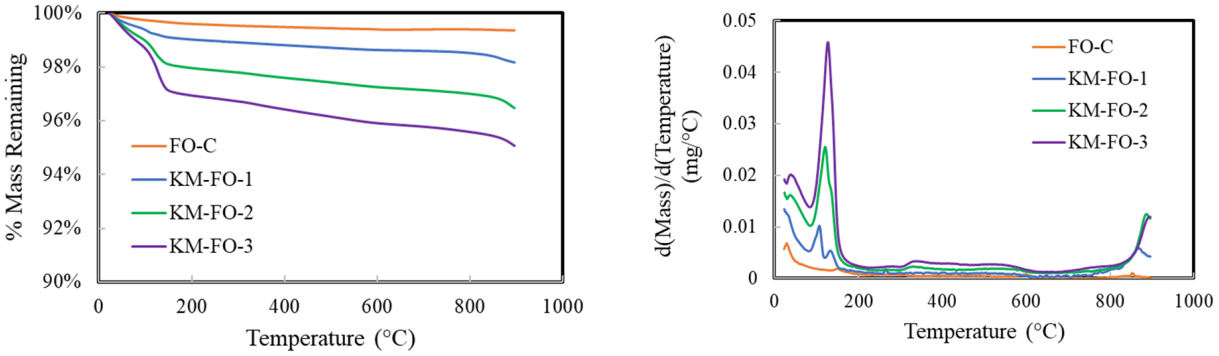


Figure 8. SEM micrographs of (**a**) MO-C, (**b**) KM-MO-1, (**c**) KM-MO-2, (**d**) KM-MO-3.

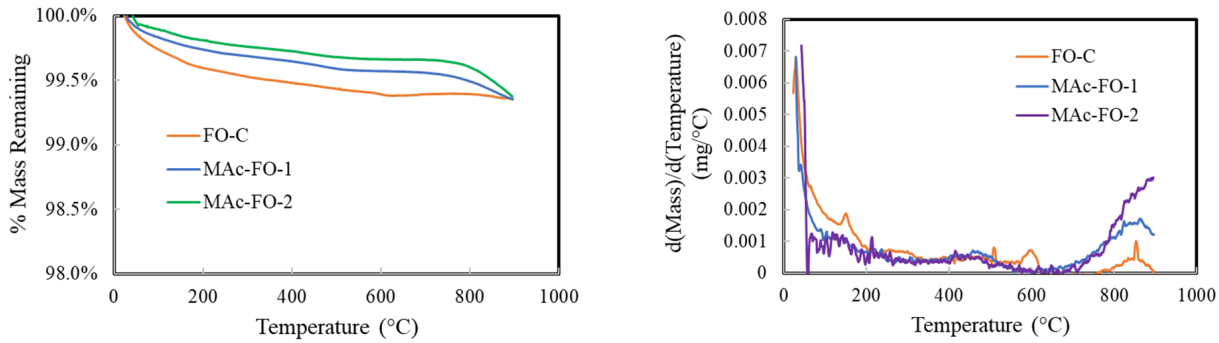
TGA analyses of KM-FO-X catalysts are shown in Figure 9a,b. Based upon the TGA profiles, as K/MnO_x increases, the loss of mass from the catalysts increases with increasing temperature. Mass losses at temperatures < 200 °C represent the desorption of water, whereas the mass lost at temperature > 800 °C likely represent the loss of oxygen due to changes in crystal phase of the K/MnO_x and MnO_x structures in the catalysts. The TGA analyses show that the presence of K on the catalysts enhances the adsorption of water vapor. This is supported by Greluk, et al. [32], who concluded that a role of K-doping of catalysts was to enhance the adsorption–dissociation of water molecules on the surface of the catalyst. The observed mass losses between 200 °C and 750 °C are likely due to losses of lattice oxygen from the K/MnO_x structures. This is supported by Almquist, et al. [42] who also observed similar mass losses with temperature on cryptomelane samples.



(**a**) (**b**)

Figure 9. TGA analyses of KM-FO-X catalysts in a nitrogen atmosphere. (**a**) % mass remaining vs temperature; (**b**) derivative of mass loss with temperature as a function of temperature.

TGA analyses of MAc-FO-X catalysts are shown in Figure 10a,b. In these samples, less than 1% of the catalyst mass was lost when temperatures increased from room temperature to 900 °C. Based upon the TGA profiles, the thermal stabilities of the MAc-FO-X catalysts were similar to that of FO-C. A comparison of Figure 10a,b with Figure 9a,b indicates that the K/MnO_x species on the catalysts are responsible for the mass losses with temperature more so than FeO_x or MnO_x alone. In addition, the loss of mass at temperatures higher than 800 °C is due to the loss of oxygen as Mn_2O_3 changes phase to Mn_3O_4 [66].



(**a**) (**b**)

Figure 10. TGA analyses of Mac-FO-X catalysts in a nitrogen atmosphere. (**a**) % mass remaining vs temperature; (**b**) derivative of mass loss with temperature as a function of temperature.

TGA analyses of KM-MO-X catalysts are shown in Figure 11a,b. Based upon the TGA profiles, as K/MnO_x increases, the mass loss from the catalyst also increases. Similarly to the KM-FO-X catalysts, the presence of potassium appears to promote the adsorption of water, as indicated by mass losses at temperatures < 200 °C. While minor mass losses were observed from the KM-MO-X catalysts between 200 °C and 600 °C, the presence of K/MnO_x on the catalysts appeared to decrease their thermal stability. At temperatures higher than 600 °C, there appeared to be three temperature regions at which mass was lost from KM-MO-X catalysts: 600–750 °C; 750–850 °C, 850–900 °C. According to a study by Stelmachowski, et al. [66], as temperature increases from 600 °C to > 900 °C, crystal phase changes in MnO_x occur due to the loss of oxygen from the catalyst. For example, with increasing temperature, $Mn_2O_3 \rightarrow Mn_3O_4 \rightarrow MnO$ and $KMn_8O_{16} \rightarrow K_xMn_4O_8$. At temperatures near 900 °C, there may also be a loss of K from the catalysts [66].

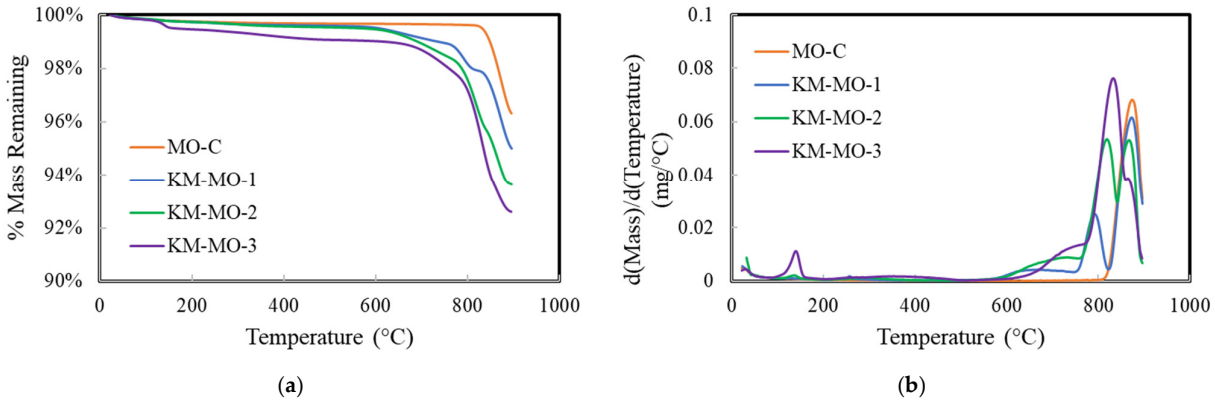


Figure 11. TGA analyses of KM-MO-X catalysts in a nitrogen atmosphere. (**a**) % mass remaining vs temperature; (**b**) derivative of mass loss with temperature as a function of temperature.

Figure 12a compares the EPR spectra of KM-FO-1, MAc-FO-1, and FO-C. FO-C exhibits very little evidence of unpaired electrons. However, KM-FO-1 and MAc-FO-1 have broad peaks. The breadth of the signals gives evidence of unpaired electrons that are either delocalized or the density of unpaired electrons is sufficiently high that ferromagnetic resonance (FMR) may be occurring. MAc-FO-1 appears to break up the interactions responsible for the broad signal of KM-FO-1, consistent with the oxidation of an Mn-O unit, which could be viewed as a partial oxygen vacancy.

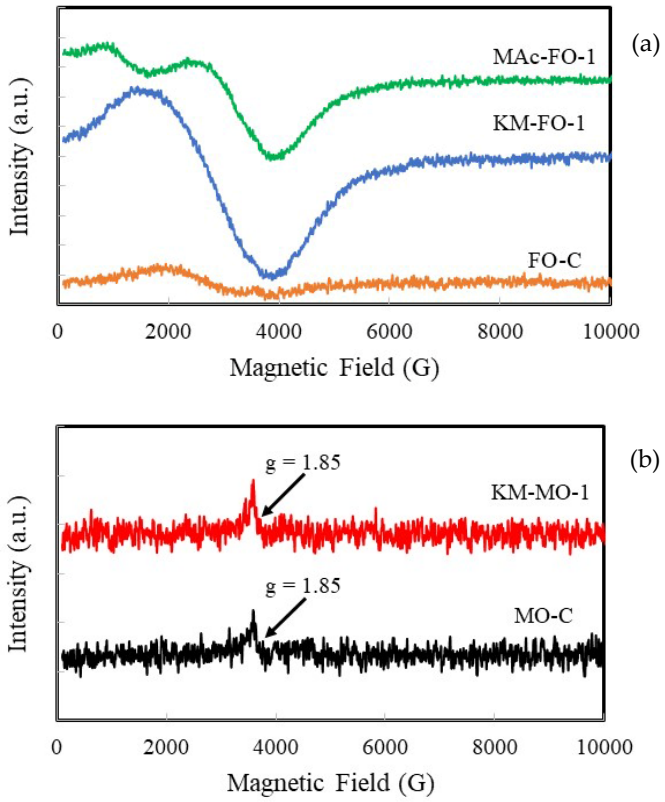


Figure 12. EPR analyses of selected catalysts used in this study. (**a**) EPR of MAc-FO-1, KM-FO-1, and FO-C. (**b**) EPR of KM-MO-1 and MO-C.

When compared to the EPR spectra for Fe^{3+} ions in glass [67], g-values of ~2.02 and g ≈ 4.2 were apparent in MAc-FO-1. For molecular or isolated Fe^{3+} species, the g ~ 4.2 is symbolic of randomly oriented, rhombically symmetric Fe^{3+}, while a signal near g ~ 2 is more consistent with a well-defined structure. According to Song, et al. [68], the EPR

signal for unpaired electrons due to oxygen vacancies occurs at around g = 2.0 [68], which is approximately the zero-crossing in both the KM-FO-1 and Mac-FO-1 spectra. Overall, the EPR spectra for KM-FO-1 and MAc-FO-1 give evidence of oxygen vacancies.

Figure 12b compares the EPR spectra of KM-MO-1 and MO-C. Both KM-MO-1 and MO-C catalysts give a similar peak at 3715 G magnetic field with g-values of 1.85. This g-value indicates that there is a possibility of oxygen vacancies around manganese [69]. The presence of K in KM-MO-1 did not appear to significantly affect the presence of unpaired electrons in the catalysts, neither of which gave evidence of a large density of unpaired electrons.

3.2. Catalyst Performance

The catalytic performance results for the deep oxidation of cyclohexane vapor are shown in Figures 13–15. In Figure 13a,b, the effect of K/MnO_x loading on FeO_x and MnO_x, respectively, are shown. The addition of K/MnO_x to FeO_x and to MnO_x increased their catalytic activity. However, in both cases, as K/MnO_x loadings increased from 0.63 mmole/g to 2.53 mmole/g, the catalytic performance decreased. These results demonstrate the promotional effects of K on MnO_x catalysts at low concentrations, but excessive loadings of K are detrimental to catalyst activity. These results coupled with the XRD and SEM results show that K alters the crystal structures, increases deposits on the catalyst surface, and alters the surface chemistry of the catalysts.

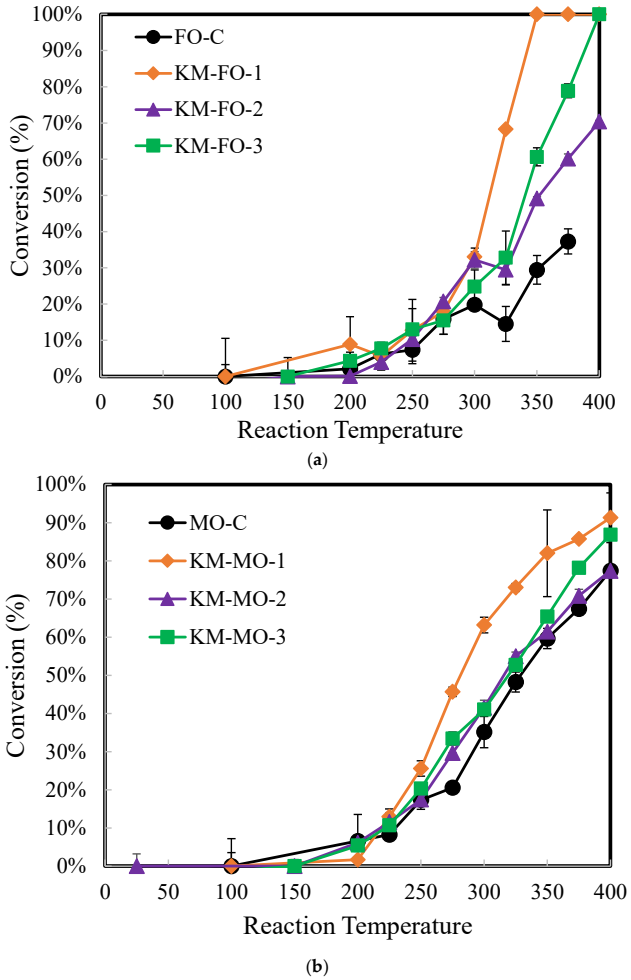


Figure 13. Effect of K/MnO_x loading on (**a**) FeO_x-supported catalysts. (**b**) MnO_x-supported catalysts. Inlet concentration = 230 ppm, catalyst mass = 50 mg; WHSV = 60 L g^{-1} h^{-1}, operating time at reaction temperature < 2 h.

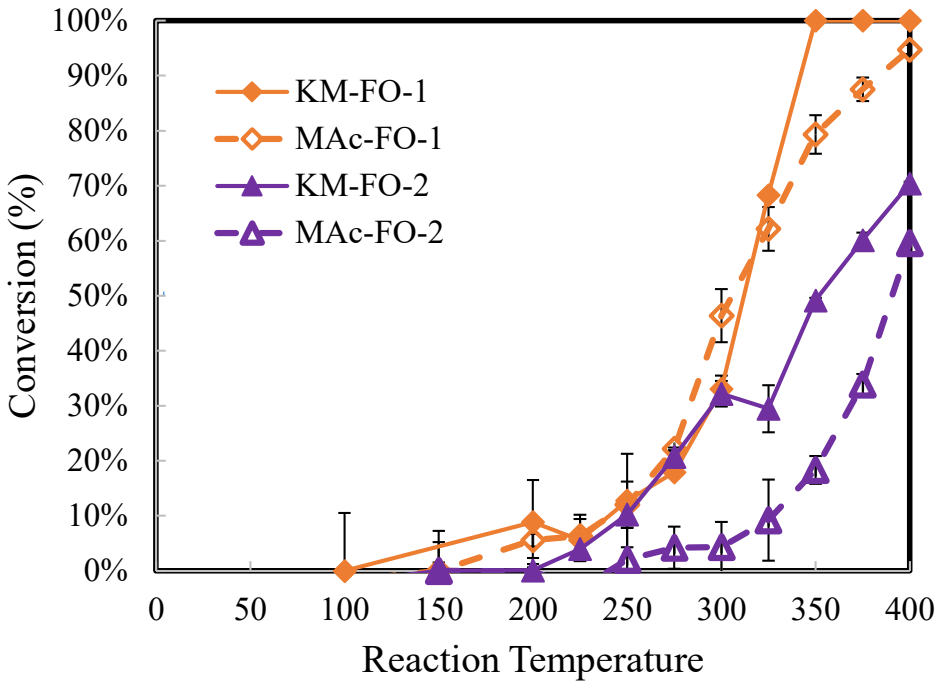


Figure 14. Comparison of FeO_x-supported MnO_x-based catalysts with and without K. Inlet concentration = 230 ppm, 50 mg catalyst, WHSV = 60 L g^{-1} h^{-1}.

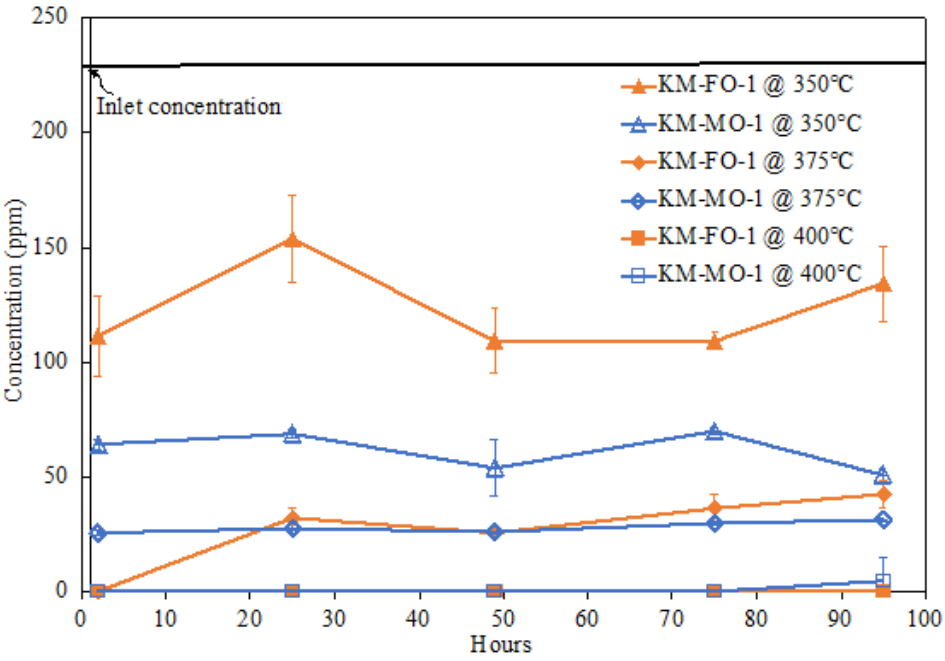


Figure 15. Catalytic activity of KM-FO-1 and KM-MO-1for 95 h of continuous operation. Inlet concentration = 230 ppm, 50 mg catalyst, WHSV = 60 L g^{-1} h^{-1}.

Figure 14 compares KM-FO-1 and KM-FO-2 with MAc-FO-1 and MAc-FO-2, respectively. In both cases, the catalysts that contained K, but similar loadings of Mn performed better than catalysts without K loadings. Reasons for the higher catalytic activity for catalysts containing K may include higher surface areas, changes in Mn crystallinity, and differences in the distribution of Mn and Fe valence states. In addition, the catalytic activities decreased with increasing Mn loadings for both KM-MO-X and MAc-MO-X catalysts. This can happen because higher Mn loadings may result in greater aggregation, less dispersion, and, therefore, less Fe-Mn interaction on the surface of the catalysts.

Table 3 summarizes the light-off temperatures (T_{50}) and activated energies calculated for the oxidation of cyclohexane over each catalyst. The light-off temperatures are defined here as the reaction temperatures at which 50% of the cyclohexane is oxidized with each catalyst. The light-off temperatures for KM-MO-X and KM-FO-X catalysts were lower than their corresponding supports (MO-C and FO-C, respectively). The trends in the light-off temperatures correlated with the catalytic performance results. Only one catalyst, MAc-FO-2, had a higher light-off temperature than its support, FO-C. Reasons may include that higher loadings of MAc to FeO_x catalysts change the valence state of Mn and Fe at the catalyst surface, thus lowering the oxygen availability and mobility. This is supported by Chen et al. [70], who found an optimal Mn/Fe molar ratio in mixed-metal oxide composite catalysts for the oxidation of toluene. They concluded that the proper ratios of Mn/Fe can improve catalyst performance due to higher amounts of Mn^{3+} ions and higher concentrations of lattice defects and oxygen vacancies [70].

Table 3. Light-off temperature (T_{50}) and activation energy.

Catalyst	T_{50} [1] (°C)	Activation Energy (kJ/mole)
FeO_x-supported catalysts		
FO-C	376	53.7
KM-FO-1	293	52.8
KM-FO-2	350	53.4
KM-FO-3	337	51.8
MAc-FO-1	306	52.4
MAc-FO-2	391	60.7
MnO_x-supported catalysts		
MO-C	326	52.1
KM-MO-1	281	49.2
KM-MO-2	313	50.3
KM-MO-3	314	50.4

[1] T_{50} is the temperature at 50% cyclohexane degradation.

Cyclohexane reacts with oxygen according to the stoichiometric reaction:

$$C_6H_{12} + 9O_2 \rightarrow intermediates \rightarrow 6CO_2 + 6H_2O$$

According to a study by Lui et al. [71], the catalytic oxidation of cyclohexane proceeds by either a chain-opening mechanism to form straight-chained alkenes and olefins, or by hydrogen abstraction to form cycloalkenes, aromatics, and aromatic oxygenates. Yadav et al. [51], also conducted a detailed spectroscopic kinetic study of the mechanism of cyclohexane oxidation. In that work, the adsorption, oxidation, and formation of cyclohexane and several oxidation by-products were considered, including cyclohexanol, cyclohexanone, and cyclohexene, among others. They concluded that their model follows a pseudo-first-order reaction with cyclohexane at low conversions [51]. Therefore, in this study, the activation energy was calculated by first assuming a first-order reaction (Equation (2)) with cyclohexane, because oxygen is present as a reactant in significant excess (~100 times the stoichiometrically required molar amount). The first-order reaction expression was integrated, assuming a plug-flow reactor, to calculate the reaction rate

constant, k (Equation (3)). The reaction rate constant, k, was used in the Arrhenius equation (Equation (4)), which was linearized to calculate the activation energy (Equation (5)).

$$rate = -\frac{dC_A}{dt} = kC_A \quad (2)$$

The rate of the reaction is in units of moles L^{-1} min^{-1}, C_A is the concentration of cyclohexane in air (moles/L), t is time (min), and k is the reaction rate constant (min^{-1}).

Assuming a plug-flow reactor, where time is residence time in the reactor, the equation is integrated, and k is determined as follows:

$$k = \frac{ln\left(\frac{C_A}{C_{Ao}}\right)}{(V/Q)} \quad (3)$$

where Q is the volumetric flow rate of the influent air stream (L min^{-1}), and V is the reactor volume (L). Equation (4) is the Arrhenius equation, which equates the reaction rate constant, k, to the activation energy, EA, of the reaction.

$$k = Ae^{-\frac{E_A}{RT}} \quad (4)$$

In Equation (4), A is the pre-exponential factor (min^{-1}), EA is the activation energy (kJ/mole), R is the gas constant (0.008314 kJ/mole/K), and T is the temperature (K). A linearized form of Equation (4) is provided in Equation (5):

$$\ln(k) = \ln(A) - \left(\frac{E_A}{R}\right)\frac{1}{T} \quad (5)$$

For each catalyst, the *ln(k)* was plotted as a function of *1/T* at conversions < 20%, and a straight line was obtained with a slope of $-E_A/R$. The pre-exponential factor for this effort was estimated to be 3.27×10^6 min^{-1}. The activation energy for cyclohexane oxidation over each catalyst was calculated based upon the slope of these graphs, and the results are provided in Table 3.

The activation energies of the FeO_x-supported catalysts are generally higher than those of the MnO_x-supported catalysts (~53 kJ/mole compared to ~50 kJ/mole), and the activation energies are relatively unaffected by the K/MnO_x loadings. The activation energies calculated here are supported by those reported by Yadav et al. [51] for cyclohexane to cyclohexanol (44 kJ/mole) [51]. In addition, Zhang et al. [72] also found the activation energy for cyclohexane oxidation to be 46.4 kJ/mole and 68.7 kJ/mole on Au/NaX zeolite catalysts. In this study, the activation energies for the oxidation of cyclohexane over KM-FO-X and KM-MO-X catalysts are comparatively lower than those obtained for their corresponding calcined supports (FO-C and MO-C, respectively). One exception is that the activation energy of MAc-FO-2 is significantly higher (~60 kJ/mole) than those of other FeO_x-supported catalysts. As discussed above, possible reasons include changes in the valence state of Mn at the catalyst surface and the lowering the oxygen availability and mobility [70]. In addition, the catalyst composition can affect the adsorption and desorption characteristics of reactants and by-products, which will ultimately affect the apparent catalytic activity of the catalyst.

The catalytic performance of KM-FO-1 and KM-MO-1 were investigated for 95 h of continuous operation at 350 °C, 375 °C, and at 400 °C, as shown in Figure 15. The inlet cyclohexane concentration was approximately 230 ppm for all trials. At 350 °C, KM-MO-1 was more active than KM-FO-1. This is contrary to the screening results, which showed KM-FO-1 performed better than KM-MO-1 at 350 °C (Figure 13a,b). A possible reason for

this observation is that KM-FO-1 is initially more active as a fresh catalyst, but after a short time, the activity decreases, possibly due to changes in the catalyst properties with time and temperature, build-up of organic by-products, or adsorption of water vapor on the catalyst surface. An initial decrease in catalyst activity was also observed with KM-FO-1 at 375 °C, where the catalytic activity at 2 h was higher than that at 25 h of operation. KM-MO-1 showed no deactivation over 95 h of operation at 350 °C or 375 °C, as indicated by a relatively constant conversion of cyclohexane. At 400 °C, no indications of catalyst deactivation were observed for either catalyst, and the conversion of cyclohexane was greater than 99.5%.

Carbon balances were conducted for the longevity trials, and the results are summarized in Table 4. In these balances, only cyclohexane and CO_2 were considered. The carbon balances at 350 °C and 375 °C were greater than 80%. Deviations from a perfect carbon balance may be due to the formation of partial oxidation by-products that were not measured or observed and error inherent in the CO_2 m. However, at 400 °C, the carbon balances were significantly lower at 67% and 69% for KM-FO1 and KM-MO-1, respectively. The relatively low carbon balances at 400 °C are most likely due to the presence of partial oxidation products that were not measured in this study. For example, carbon monoxide was not measured in this study. Also, there were some observable organic by-products in the effluent stream, but they were not measurable due to their small peak areas (GC peak areas < 1 picoamp·min). In addition, carbon build-up on the catalyst may have occurred.

Table 4. Carbon balances for trials over 95 h of continuous operation.

Catalyst	Temperature (°C)	Cyclohexane (ppm)			CO_2 (ppm)	$^1C_{out}/C_{in}$
		In	Out	Conversion	Out	
KM-FO-1	350	208	124	40%	251	80%
	375	201	27	87%	957	93%
	400	213	0	100%	863	67%
KM-MO-1	350	231	61	74%	904	92%
	375	220	28	87%	1083	95%
	400	239	1	99.6%	991	69%

^{1}C = moles of carbon in cyclohexane and in CO_2.

In Figure 16, the FTIR spectra of unused and used catalysts (after 95 h of continuous operation at 400 °C) are compared. The used catalysts have absorption peaks that represent organic functional groups on the catalyst surface. This indicates that partial oxidation products were formed and adhered to the surface of the catalysts. They are more prominent for KM-FO-1 than for KM-MO-1, indicating that there was more build-up of partial oxidation products on KM-FO-1 than on KM-MO-1. In a study by Einaga and Futamura (2005), several partial oxidation species of cyclohexane were identified using FTIR on alumina-supported manganese oxides. They included ketones, alcohols, carboxylic acids, and acid anhydrides, among others [73]. The organic by-products retained on the catalyst surface may have accounted for the decrease in apparent catalytic activity as well as the carbon balance. In addition, the broad peak between 3000 cm^{-1} and 3700 cm^{-1} on KM-FO-1 compared to KM-MO-1 suggests that KM-FO-1 adsorbs water to a greater extent, which may also account for the decrease in apparent catalytic activity. Water vapor would compete with cyclohexane for adsorption sites on the catalyst surface.

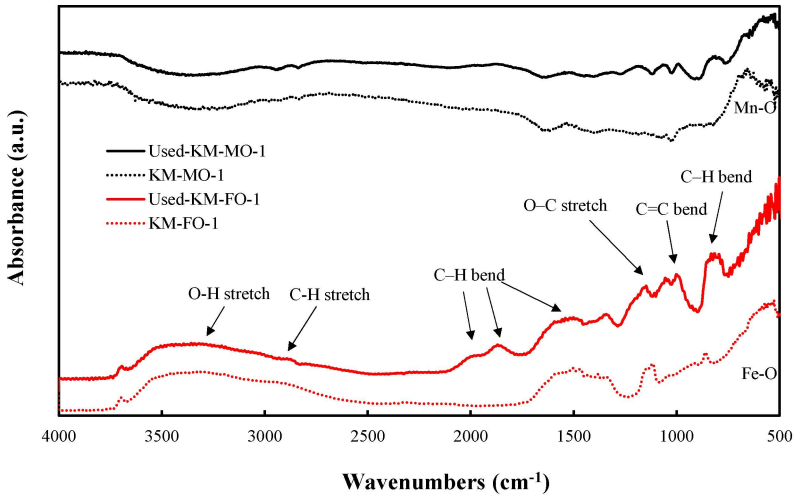


Figure 16. FTIR spectrum of used and un-used KM-FO-1 and KM-MO-1 catalysts after 95 h of continuous operation at 400 °C. The organic functional groups corresponding to the FTIR peaks were identified by comparison with a FTIR reference table [56].

4. Discussion

In a review by James Spivey (1987), generalizations were made regarding the catalytic activity of metal oxides for VOC oxidation [16]. This review highlighted that the high activity of metal oxides is related to the metal having more than one valence state and the catalyst having highly mobile surface oxygen. He further stated that Mn and Fe would be among the most active metal oxide catalysts due to their multiple valence states and redox properties [16].

The efforts of this study were to investigate K/MnO_x catalysts supported on FeO_x and MnO_x for the deep oxidation of cyclohexane. There are two key aspects of this study: (1) the effect of K on MnO_x catalysts, and (2) the effect of FeO_x as a support for K/MnO_x and MnO_x catalysts. Each of these aspects are discussed in more detail below.

4.1. The Effect of K on MnO_x Catalysts

In this study, the effects of K on MnO_x catalysts included the following: inhibition of changes in the crystallinity and crystal phase of the catalyst support, increased propensity for water adsorption, formation of K/MnO_x crystalline species on the catalyst support, decreased thermal stability, and enhanced catalytic activity over catalysts of similar composition but without K. These effects were evidenced by experimental observations in this study, and they are supported by previously published studies. XRD and EPR results give indications that the catalysts contain mixed valence states of Mn and Fe and oxygen vacancies, which could enhance catalytic activity. These results are supported by Zheng et al. [19], where the authors reported that ion-doping of MnO_x can have significant effects on catalyst properties and activities. For example, the introduction of K to the catalyst can affect the electronic and geometric structures of the catalysts, and so enhance surface oxygen activity and facilitate the regeneration of surface hydroxyl species through activation of water. In a study by Greluk et al. [32], a significant increase in catalyst stability with the addition of K was observed. They concluded that the potassium favored the adsorption and dissociation of water molecules and, therefore, enhanced the oxidation of soot build-up on the catalysts. Lui et al. [71] reported that the promotion mechanism of K to Mn-based catalysts is the formation of defect oxides, which have higher mobility than lattice oxygen species, and hence, higher catalytic activity.

It was also observed in this study that as the K/MnO_x loading on FeO_x and MnO_x increased from 0.63 mmoles/g support to 2.53 mmoles/g support, the catalytic activity

decreased. This result is supported by Zheng et al. [19], who state that excessive K would cause oxygen to become more stable and less mobile. In addition, the interactions of K with adsorbed carbon dioxide (CO_2) may decrease the activity by decreasing the rate of desorption of CO_2 from the surface of the catalyst [19]. The addition of K also changes the morphology and crystal structure of the catalyst, which was evident in the SEM micrographs presented in Figures 6–8. These, too, could be reasons for the catalytic activity to decrease with increasing K/MnO_x loading.

4.2. The Effect of FeO_x as a Support for K/MnO_x-Based and MnO_x-Based Catalysts

Catalyst supports can provide high specific surface area, a stable structure, and a pore structure that is conducive to dispersion of active sites on a catalyst surface [21]. In this study, however, the FeO_x-supported catalysts generally had lower catalytic activity than the K/MnO_x-based catalysts on MnO_x supports, even though the BET surface areas of the KM-FO-X catalysts were higher than those of KM-MO-X catalysts. In addition, the lowest loadings of K/MnO_x and MnO_x on FeO_x (0.63 mmoles/g support) had the highest catalytic activities of the FeO_x-supported catalysts in this study. MAc-FO-1 and KM-FO-1 had similar activities at temperatures up to 325 °C, indicating that the MnO_x-species on the FeO_x support is the active species. The FTIR spectra of used catalysts, however, indicate that the FeO_x-supported catalysts had more organic build-up following extended continuous operation than MnO_x-supported catalysts.

5. Conclusions

This research underscores the relationship between catalyst composition, support material, K/MnO_x loading levels, and catalytic performance of K/MnO_x- and MnO_x-based catalysts, providing insights for the design of more effective catalysts for volatile organic compound (VOC) oxidation. The presence of K on MnO_x catalysts significantly enhanced the apparent catalytic activity for the deep oxidation of cyclohexane. Mixed crystal structures in the supports indicate that Fe and Mn have a distribution of valence states, which would result in redox reactions at the interface of FeO_x and MnO_x structures, oxygen defects, and ultimately enhanced catalytic activity for VOC oxidation.

In this study, the K/MnO_x catalysts supported on MnO_2 performed better than those with similar K/MnO_x loadings supported on Fe_3O_4 for the deep oxidation of cyclohexane. The activation energies for MnO_2-supported catalysts and Fe_3O_4-supported catalysts were approximately 50 kJ/mole and 53 kJ/mole, respectively. The catalysts containing the lowest loadings of K/MnO_x (0.63 mmoles/g support) resulted in the highest catalytic activity for both MnO_2^- and $Fe_3O_4^-$ supported catalysts. Changes in surface structure, morphology, valence states of Fe and Mn, and water adsorption properties, as evidenced by experimental observations in this study, are possible reasons for a decrease in the apparent catalytic activity as K/MnO_x and MnO_x loadings increase.

Supplementary Materials: The following supporting information can be downloaded at: https://www.mdpi.com/article/10.3390/pr13030634/s1.

Author Contributions: Conceptualization, M.S.K. and C.B.A.; methodology, M.S.K., D.L.T. and C.B.A.; software, M.S.K.; formal analysis, M.S.K., D.L.T. and C.B.A.; investigation, M.S.K.; resources, M.S.K. and C.B.A.; data curation, M.S.K.; writing—original draft preparation, M.S.K.; writing—review and editing, C.B.A. and D.L.T.; visualization, M.S.K. and C.B.A.; supervision, C.B.A.; project administration, C.B.A. All authors have read and agreed to the published version of the manuscript.

Funding: This research received no external funding.

Data Availability Statement: The data that support the findings of this study are available from the corresponding author upon reasonable request.

Acknowledgments: The following personnel at Miami University are acknowledged for their assistance as this study was conducted: the Chemical, Paper, and Biomedical Engineering Department at Miami University for research support; Marion Lytle for training and assistance with XRD analyses, and Douglas Hart for general laboratory support. We also acknowledge the support of the staff and resources from the Center for Advanced Microscopy and Imaging (CAMI) at Miami University.

Conflicts of Interest: The authors declare no conflicts of interest.

References

1. Zhou, X.; Zhou, X.; Wang, C.; Zhou, H. Environmental and human health impacts of volatile organic compounds: A perspective review. *Chemosphere* **2023**, *313*, 137489. [CrossRef] [PubMed]
2. Technical Overview of Volatile Organic Compounds, US EPA. Available online: https://www.epa.gov/indoor-air-quality-iaq/technical-overview-volatile-organic-compounds (accessed on 5 January 2025).
3. Baskaran, D.; Dhamodharan, D.; Behera, U.S.; Byun, H.-S. A comprehensive review and perspective research in technology integration for the treatment of gaseous volatile organic compounds. *Environ. Res.* **2024**, *251*, 118472. [CrossRef] [PubMed]
4. Annual Volatile Organic Compounds (VOC) Emissions in the United States from 1970 to 2023. Available online: https://www.statista.com/statistics/501310/volume-of-volatile-organic-compounds-emissions-us/ (accessed on 5 January 2025).
5. De Alwis, D.; Limaye, V.S. The Costs of Inaction: The Economic Burden of Fossil Fuels and Climate Change on Health in the United States. National Resource Defense Council and The Medical Society Council on Climate and Health. 2021. Available online: https://www.nrdc.org/sites/default/files/costs-inaction-burden-health-report.pdf (accessed on 23 December 2024).
6. Fu, N.; Cao, L.-M.; Xia, S.-Y.; Zeng, L.-W.; He, L.; He, L.-Y.; Huang, X.-F. Sensitivity of atmospheric peroxyacetyl nitrate (PAN) formation and its impact on ozone pollution in a coastal city. *Atmos. Environ.* **2024**, *330*, 120545. [CrossRef]
7. Movassaghi, K.; Russo, M.V.; Avino, P. The determination and role of peroxyacetil nitrate in photochemical processes in atmosphere. *Chem. Cent. J.* **2012**, *6* (Suppl. S2), S8. [CrossRef] [PubMed]
8. Khan, F.I.; Ghoshal, A.K. Removal of volatile organic compounds from polluted air. *J. Loss Prev. Process Ind.* **2000**, *13*, 527–545. [CrossRef]
9. Sorrels, J.L.; Baynham, A.; Randall, D.; Hancy, C. Incinerators and Oxidizers. In *Cost Reports and Guidance for Air Pollution Regulations, Economic and Cost Analysis for Air Pollution Regulations*; Research Triangle Institute: Research Triangle Park, NC, USA, 2017; Chapter 2. Available online: https://www.epa.gov/sites/default/files/2017-12/documents/oxidizersincinerators_chapter2_7theditionfinal.pdf (accessed on 5 January 2025).
10. Air Pollution Control Technology Fact Sheet. US EPA. Available online: https://www3.epa.gov/ttn/catc/dir1/fthermal.pdf (accessed on 5 January 2025).
11. Yang, C.; Miao, G.; Pi, Y.; Xia, Q.; Wu, J.; Li, Z.; Xiao, J. Abatement of various types of VOCs by adsorption/catalytic oxidation: A review. *Chem. Eng. J.* **2017**, *370*, 1128–1153. [CrossRef]
12. Kamal, M.S.; Razzak, S.A.; Hossain, M.M. Catalytic oxidation of volatile organic compounds (VOCs)—A review. *Atmos. Environ.* **2016**, *140*, 117–134. [CrossRef]
13. Gelles, T.; Krishnamurthy, A.; Adebayo, B.; Rownaghi, A.; Rezaei, F. Abatement of gaseous volatile organic compounds: A material perspective. *Catal. Today* **2020**, *350*, 3–18. [CrossRef]
14. Wang, P.; Wang, L.; Zhao, Y.; Zhang, B.; Wang, D. Progress in Degradation of Volatile Organic Compounds by Catalytic Oxidation: A Review Based on the Kinds of Active Components of Catalysts. *Water Air Soil Pollut.* **2023**, *235*, 7. [CrossRef]
15. Liu, R.; Wu, H.; Shi, J.; Xu, X.; Zhao, D.; Ng, Y.H.; Zhang, M.; Liu, S.; Ding, H. Recent progress on catalysts for catalytic oxidation of volatile organic compounds: A review. *Catal. Sci. Technol.* **2022**, *12*, 6945–6991. [CrossRef]
16. Spivey, J.J. Complete catalytic oxidation of volatile organics. *Ind. Eng. Chem. Res.* **1987**, *26*, 2165–2180. [CrossRef]
17. Liotta, L.F. Catalytic oxidation of volatile organic compounds on supported noble metals. *Appl. Catal. B Environ.* **2010**, *100*, 403–412. [CrossRef]
18. Li, B.; Wang, J.X.; Gong, H. Catalytic combustion of VOCs on non-noble metal catalysts. *Catal. Today* **2009**, *148*, 81–87. [CrossRef]
19. Zheng, J.; Zhao, W.; Song, L.; Wang, H.; Yan, H.; Chen, G.; Han, C.; Zhang, J. Advances of manganese-oxides-based catalysts for indoor formaldehyde removal. *Green Energy Environ.* **2023**, *8*, 626–653. [CrossRef]
20. Li, X.; Zhang, J.; Zhang, Y.; Liu, B.; Liang, P. Catalytic oxidation of volatile organic compounds over manganese-based catalysts: Recent trends and challenges. *J. Environ. Chem. Eng.* **2022**, *10*, 108638. [CrossRef]
21. Zhou, H.; Su, W.; Xing, Y.; Wang, J.; Zhang, W.; Jia, H.; Su, W.; Yue, T. Progress of catalytic oxidation of VOCs by manganese-based catalysts. *Fuel* **2024**, *366*, 131305. [CrossRef]

22. Zhou, Y.H.; Lei, X.X.; Zhou, J.Y.; Yan, D.L.; Deng, B.; Liu, Y.D.; Xu, W.L. Recent Advances in the Regulation of Oxygen Vacancies in MnO_2 Nanocatalysts. *Catal. Surv. Asia* **2023**, *27*, 319–331. [CrossRef]
23. Genuino, H.C.; Dharmarathna, S.; Njagi, E.C.; Mei, M.C.; Suib, S.L. Gas-Phase Total Oxidation of Benzene, Toluene, Ethylbenzene, and Xylenes Using Shape-Selective Manganese Oxide and Copper Manganese Oxide Catalysts. *J. Phys. Chem. C* **2012**, *116*, 12066–12078. [CrossRef]
24. Figueredo, M.J.M.; Cocuzza, C.; Bensaid, S.; Fino, D.; Piumetti, M.; Russo, N. Catalytic Abatement of Volatile Organic Compounds and Soot over Manganese Oxide Catalysts. *Materials* **2021**, *14*, 4534. [CrossRef]
25. Wu, P.; Jin, X.; Qiu, Y.; Ye, D. Recent Progress of Thermocatalytic and Photo/Thermocatalytic Oxidation for VOCs Purification over Manganese-based Oxide Catalysts. *Environ. Sci. Technol.* **2021**, *55*, 4268–4286. [CrossRef]
26. Lu, T.; Su, F.; Zhao, Q.; Li, J.; Zhang, C.; Zhang, R.; Liu, P. Catalytic oxidation of volatile organic compounds over manganese-based oxide catalysts: Performance, deactivation and future opportunities. *Sep. Purif. Technol.* **2022**, *296*, 121436. [CrossRef]
27. Xu, Z.; Li, Y.; Shi, H.; Lin, Y.; Wang, Y.; Wang, Q.; Zhu, T. Application Prospect of K Used for Catalytic Removal of NOx, COx and VOCs from Industrial Flue Gas: A Review. *Catalysts* **2021**, *11*, 419. [CrossRef]
28. Zhu, Q.; Jiang, Z.; Ma, M.; He, C.; Yu, Y.; Liu, X.; Albilali, R. Revealing the unexpected promotion effect of diverse potassium precursors on α-MnO_2 for the catalytic destruction of toluene. *Catal. Sci. Technol.* **2020**, *10*, 2100–2110. [CrossRef]
29. Zhang, X.; Yang, Y.; Zhu, Q.; Ma, M.; Jiang, Z.; Liao, X.; He, C. Unraveling the effects of potassium incorporation routes and positions on toluene oxidation over α-MnO_2 nanorods: Based on experimental and density functional theory (DFT) studies. *J. Colloid Interface Sci.* **2021**, *598*, 324–338. [CrossRef]
30. Li, H.; Song, Z.; Zhang, Z.; Zhang, X.; Mao, Y.; Liu, W.; Huang, Z.; Zhang, J.; Dong, D.; Luo, Y. Catalytic combustion of toluene performance over MnO catalysts: Effect of KMnO4 content. *Appl. Organomet. Chem.* **2024**, *38*, e7388. [CrossRef]
31. Lai, X.; Feng, J.; Zhou, X.; Hou, Z.; Lin, T.; Chen, Y. Catalytic Oxidation of Toluene Over Potassium Modified $Mn/Ce_{0.65}Zr_{0.35}O_2$ Catalyst. *Acta Phys. Chim. Sin.* **2020**, *36*, 1905047. [CrossRef]
32. Greluk, M.; Rotko, M.; Słowik, G.; Turczyniak-Surdacka, S.; Grzybek, G.; Tyszczuk-Rotko, K. Effect of Potassium Doping on the Structural and Catalytic Properties of Co/MnOx Catalyst in the Steam Reforming of Ethanol. *Materials* **2023**, *16*, 5377. [CrossRef]
33. Santos, V.P.; Pereira, M.F.R.; Orfao, J.J.M.; Figueiredo, J.L. Mixture effects during the oxidation of toluene, ethyl acetate, and ethanol over a cryptomelane catalyst. *J. Hazard. Mater.* **2011**, *185*, 1236–1240. [CrossRef]
34. Santos, V.P.; Soares, O.S.G.P.; Bakker, J.J.W.; Pereira, M.F.R.; Orfao, J.J.M.; Gascon, J.; Kapteijn, F.; Figueiredo, J.L. Structural and chemical disorder of cryptomelane promoted by alkali doping: Influence on catalytic properties. *J. Catal.* **2012**, *293*, 165–174. [CrossRef]
35. Peluso, M.A.; Pronsato, E.; Sambeth, J.E.; Thomas, H.J.; Busca, G. Catalytic combustion of ethanol on pure and alumina supported K-Mn oxides: An IR and flow reactor study. *Appl. Catal. B Environ.* **2008**, *78*, 73–79. [CrossRef]
36. Peluso, M.A.; Gambaro, L.A.; Pronsato, E.; Giazzoli, D.; Thomas, H.J.; Sambeth, J.E. Synthesis and catalytic activity of manganese dioxide (type OMS-2) for the abatement of oxygenated VOCs. *Catal. Today* **2008**, *133*, 487–492. [CrossRef]
37. Santos, V.P.; Pereira, M.R.F.; Orfai, J.J.M.; Figueiredo, J.I. The role of lattice oxygen on the activity of manganese oxides towards the oxidation of volatile organic compounds. *Appl. Catal. B Environ.* **2010**, *99*, 353–363. [CrossRef]
38. Santos, V.P.; Bastos, S.S.T.; Pereira, M.F.R.; Orfao, J.J.M.; Figueiredo, J.L. Stability of a cryptomelane catalyst in the oxidation of toluene. *Catal. Today* **2010**, *154*, 308–311. [CrossRef]
39. Luo, J.; Zhang, Q.; Huang, A.; Suib, S.L. Total oxidation of volatile organic compounds with hydrophobic cryptomelane-type octahedral molecular sieves. *Microporous Mesoporous Mater.* **2000**, *35–36*, 209–217. [CrossRef]
40. Vaculíková, L.; Valovičová, V.; Plevová, E.; Napruszewska, B.D.; Duraczyńska, D.; Karcz, R.; Serwicka, E.M. Synthesis, characterization and catalytic activity of cryptomelane/montmorillonite composites. *Appl. Clay Sci.* **2021**, *202*, 105977. [CrossRef]
41. Gandhe, A.R.; Rebello, J.S.; Figueiredo, J.L.; Fernandes, J.B. Manganese oxide OMS-2 as an effective catalyst for total oxidation of ethyl acetate. *Appl. Catal. B Environ.* **2007**, *72*, 129–135. [CrossRef]
42. Almquist, C.B.; Krekeler, M.; Jiang, L. An investigation on the structure and catalytic activity of cryptomelane-type manganese oxide materials prepared by different synthesis routes. *Chem. Eng. J.* **2014**, *252*, 249–262. [CrossRef]
43. Sun, H.; Chen, S.; Wang, P.; Quan, X. Catalytic oxidation of toluene over manganese oxide octahedral molecular sieves (OMS-2) synthesized by different methods. *Chem. Eng. J.* **2011**, *178*, 191–196. [CrossRef]
44. Tian, H.; He, J.; Zhang, X.; Zhou, L.; Wang, D. Facile synthesis of porous manganese oxide K-OMS-2 materials and their catalystic activity for formaldehyde oxidation. *Microporous Mesoporous Mater.* **2011**, *138*, 118–122. [CrossRef]
45. Suib, S.L. Structure, porosity, and redox in porous manganese oxide octahedral layer and molecular sieve materials. *J. Mater. Chem.* **2008**, *18*, 1623–1631. [CrossRef]
46. Hettige, C.; Mahanama, K.R.R.; Dissanayake, D.P. Cyclohexane oxidation and carbon deposition over metal oxide catalysts. *Chemosphere* **2001**, *43*, 1079–1083. [CrossRef] [PubMed]
47. Jung, S.-C.; Park, Y.-K.; Jung, H.Y.; Kang, U.I.; Nah, J.W.; Kim, S.C. Effects of calcination and support on supported manganese catalysts for the catalytic oxidation of toluene as a model of VOCs. *Res. Chem. Intermed.* **2016**, *42*, 185–199. [CrossRef]

48. Liu, Y.; Luo, M.; Wei, Z.; Xin, Q.; Ying, P.; Li, C. Catalytic oxidation of chlorobenzene on supported manganese oxide catalysts. *Appl. Catal. B Environ.* **2001**, *29*, 61–67. [CrossRef]
49. Gallardo-Amores, J.M.; Armaroli, T.; Ramis, G.; Finocchio, E.; Busca, G. A study of anatase–supported Mn oxide as catalysts for 2-propanol oxidation. *Appl. Catal. B Environ.* **1999**, *22*, 249–259. [CrossRef]
50. Duplančić, M.; Gomzi, V.; Pintar, A.; Kurajica, S.; Tomašić, V. Experimental and theoretical (ReaxFF) study of manganese-based catalysts for low-temperature toluene oxidation. *Ceram. Int.* **2021**, *47*, 3108–3121. [CrossRef]
51. Yadav, V.K.; Das, T. Oxidation of cyclohexane over supported Fe–Mn catalysts: In situ DRIFTS studies. *Phys. Chem. Chem.* **2021**, *23*, 13612–13622. [CrossRef]
52. Soltan, W.B.; Sun, J.; Wang, W.; Song, Z.; Zhao, X.; Mao, Y.; Zhang, Z. Discovering the key role of MnO_2 and CeO_2 particles in the Fe_2O_3 catalysts for enhancing the catalytic oxidation of VOC: Synergistic effect of the lattice oxygen species and surface-adsorbed oxygen. *Sci. Total Environ.* **2022**, *819*, 152844. [CrossRef]
53. Gong, P.; Cao, R.; Yu, Y.; Zhang, J. Promotion effect of SO42−/Fe2O3 modified MnOx catalysts for simultaneous control of NO and CVOCs. *Surf. Interfaces* **2022**, *33*, 102253. [CrossRef]
54. Li, Y.; Li, Y.; Wang, P.; Hu, W.; Zhang, S.; Shi, Q.; Zhan, S. Low-temperature selective catalytic reduction of NO_x with NH_3 over MnFeOx nanorods. *Chem. Eng. J.* **2017**, *330*, 213–222. [CrossRef]
55. Stelmachowski, P.; Videla, A.H.A.M.; Specchia, S.; Stelmachowski, P.; Jakubek, T.; Kotarba, A. The Effect of Fe, Co, and Ni Structural Promotion of Cryptomelane (KMn_8O_{16}) on the Catalytic Activity in Oxygen Evolution Reaction. *Electrocatalysis* **2018**, *9*, 762–769. [CrossRef]
56. Infrared Spectroscopy Adsorption Table. Available online: https://chem.libretexts.org/Ancillary_Materials/Reference/Reference_Tables/Spectroscopic%20Reference_Tables/Infrared_Spectroscopy_Absorption_Table (accessed on 5 January 2025).
57. Khan, R.H.; Rotich, N.C.; Morris, A.; Ahammad, T.; Baral, B.; Sahu, I.D.; Lorigan, G.A. Probing the Structural Topology and Dynamic Properties of gp28 Using Continuous 49 Wave Electron Paramagnetic Resonance Spectroscopy. *J. Phys. Chem. B* **2023**, *127*, 9236–9247. [CrossRef] [PubMed]
58. Quantachrome Instruments. Powder Tech Note 54, Automated Software Assistant for the Proper Calculation of BET Area of Microporous Materials. Available online: https://r.search.yahoo.com/_ylt=AwrEqhz0abtnqvcEYHFXNyoA;_ylu=Y29sbwNiZjEEcG9zAzEEdnRpZAMEc2VjA3Ny/RV=2/RE=1741545205/RO=10/RU=https://www.researchgate.net/profile/Martin-Thomas-3/post/How_can_you_calculate_micropore_surface_area_using_N2_adsorption_isotherms/attachment/59d61f5679197b807797dc7f/AS%253A284180681379842%25401444765362986/download/TechNote-54_BET+Area+of+Microporous+Solids_121911.pdf/RK=2/RS=vWl2Tc27ClvCHh78xplqMkKUReY- (accessed on 23 February 2025).
59. Kruk, M.; Jaroniec, M. Determination of the specific surface area and the pore size of microporous carbons from adsorption potential distributions. *Langmuir* **1999**, *15*, 1442–1448. [CrossRef]
60. Sing, K. The use of nitrogen adsorption for the characterization of porous materials. *Colloids Surf. A Physicochem. Eng. Asp.* **2001**, *187–188*, 3–9. [CrossRef]
61. Available online: https://ethz.ch/content/dam/ethz/special-interest/chab/icb/van-bokhoven-group-dam/coursework/Characterization-Techniques/2016/physisorption-pore-size-analysis-2016.pdf (accessed on 23 February 2025).
62. Galarneau, A.; Mehlhorn, D.; Guenneau, F.; Coasne, B.; Villemot, F.; Minoux, D.; Aquino, C.; Dath, J.-P. Specific Surface Area Determination for Microporous/Mesoporous Materials: The Case of Mesoporous FAU-Y Zeolites. *Langmuir Am. Chem. Soc.* **2018**, *34*, 14134–14142. [CrossRef]
63. Najfach, A.J.; Almquist, C.B.; Edelmann, R.E. Effect of Manganese and zeolite composition on zeolite-supported Ni-catalysts for dry reforming of methane. *Catal. Today* **2021**, *369*, 31–47. [CrossRef]
64. Birkner, N.; Navrotsky, A. Thermodynamics of manganese oxides: Sodium, potassium, and calcium birnessite and cryptomelane. *Proc. Natl. Acad. Sci. USA* **2017**, *114*, E1046–E1053. [CrossRef]
65. Mohamed, A.K. TP3—Ceramics: Sintering and Microstructure. Available online: https://www.epfl.ch/labs/lmc/wp-content/uploads/2018/08/TP3-English-2016.pdf (accessed on 15 February 2025).
66. Stelmachowski, P.; Legutko, P.; Jakubek, T.; Kotarba, A. Phase evolution and electronic properties of cryptomelane nanorods. *J. Alloys Compd.* **2018**, *767*, 592–599. [CrossRef]
67. Muralidhara, R.S.; Kesavulu, C.R.; Rao, J.L.; Anavekar, R.V.; Chakradhar, R.P.S. EPR and optical absorption studies of Fe^{3+} ions in sodium borophosphate glasses. *J. Phys. Chem. Solids* **2010**, *71*, 1651–1655. [CrossRef]
68. Song, Q.; Zhou, S.; Wang, S.; Li, S.; Xu, L.; Qiu, J. Insights into the oxygen vacancies in transition metal oxides for aqueous Zinc-Ion batteries. *Chem. Eng. J.* **2023**, *461*, 142033. [CrossRef]
69. Zhang, K.; Ding, H.; Pan, W.; Mu, X.; Qiu, K.; Ma, J.; Zhao, Y.; Song, J.; Zhang, Z. Research Progress of a Composite Metal Oxide Catalyst for VOC Degradation. *Environ. Sci. Technol.* **2022**, *56*, 9220–9236. [CrossRef]
70. Chen, J.; Chen Xi Xu, W.; Xu, Z.; Chen, J.; Jia, H.; Chen, J. Hydrolysis driving redox reaction to synthesize Mn-Fe binary oxides as highly active catalysts for the removal of toluene. *Chem. Eng. J.* **2017**, *330*, 281–293. [CrossRef]

71. Liu, Q.; Wen, M.; Guo, Y.; Song, S.; Li, G.; An, T. Efficient Catalytic Combustion of Cyclohexane over PdAg/Fe_2O_3 Catalysts under Low-Temperature Conditions: Establishing the Degradation Mechanism Using PTR-TOF-MS and in Situ DRIFTS. *ACS Appl. Mater. Interfaces* **2022**, *14*, 55503–55516. [CrossRef] [PubMed]
72. Zhang, Z.; Hu, M.; Gui, Q.; Gu, J.; Xu, W.; Xiao, Q.; Huang, W. Highly enhanced direct catalytic oxidation of cyclohexane to adipic acid with molecular oxygen: Dynamic collaboration between zeolite channel micro-environment and Au clusters. *Chem. Eng. J.* **2023**, *467*, 143501. [CrossRef]
73. Einaga, H.; Futamura, S. Oxidation behavior of cyclohexane on alumina-supported manganese oxides with ozone. *Appl. Catal. B Environ.* **2005**, *60*, 49–55. [CrossRef]

Disclaimer/Publisher's Note: The statements, opinions and data contained in all publications are solely those of the individual author(s) and contributor(s) and not of MDPI and/or the editor(s). MDPI and/or the editor(s) disclaim responsibility for any injury to people or property resulting from any ideas, methods, instructions or products referred to in the content.